Bioactive Materials 64 (2026) 589–603

Contents lists available at ScienceDirect

Bioactive Materials

journal homepage: www.keaipublishing.com/en/journals/bioactive-materials

# Degradation of biodegradable orthopedic screws does (not) elevate tissue heating under Magnetic Resonance Imaging: Implications for next generation implants

Mostafa Berangi [a,c], Helmar Waiczies [c], Nandita Saha [a,b], Shahriar Shalikar [a,b], Mahsa Salimi Majd [b], Thoralf Niendorf [a,b,c,*]

[a] Berlin Ultrahigh Field Facility (B.U.F.F.), Max-Delbrück-Center for Molecular Medicine in the Helmholtz Association, Berlin, Germany
[b] Charité—Universitätsmedizin Berlin, Belin, Germany
[c] MRI.TOOLS GmbH, Berlin, Germany

ARTICLE INFO

*Keywords:*
Biodegradable implant
MRI
Safety
Radiofrequency heating
Thermal modeling
Implant fracture
Implant degradation

ABSTRACT

Magnesium (Mg) alloy screws represent promising biodegradable orthopedic implants owing to their biocompatibility, mechanical strength, and gradual resorption, thereby obviating the need for secondary removal surgery. However, their electrical conductivity raises safety concerns during magnetic resonance imaging (MRI) used for the assessment of healing progress and potential complications, where exposure to radiofrequency (RF) energy may induce tissue heating. As Mg implants degrade, evolving geometry and material phase may alter electromagnetic behavior, deposition of RF energy and potential heating. This study systematically examined the effects of key degradation mechanisms—volume reduction, surface roughening, formation of a magnesium hydroxide layer, and implant fractures—on MRI-induced heating. High-resolution electromagnetic field simulations at 3.0 T (ASTM F2182 phantom and realistic human voxel model) were complemented by thermal modeling and experimental MRI heating measurements using real-world screws. Volume loss and edge smoothing reduced maximum 1g-specific absorption rate ($SAR_{1g}$) by up to 12%, while surface roughness (RMS = 0.5 mm) reduced SAR1g by −0.28% through increased surface impedance. Degradation layer caused minimal SAR change (<0.5%). Screw fractures increased localized $SAR_{1g}$ by up to 19.1% but redistributed heat more uniformly across the implant, lowering peak temperatures compared to intact screws. In the human voxel model, fractured screws remained below the IEC safety limits under maximum permissible RF exposure with a maximum temperature elevation of 38.9 °C, whereas non-fractured screws exceeded 40 °C. Our results demonstrate that Mg screw degradation generally mitigates MRI heating risks. In conclusion, engineered degradation features may enhance MRI safety, providing design guidance for next-generation biodegradable orthopedic implants.

## 1. Introduction

The use of biodegradable magnesium (Mg) alloys in orthopedic implants has gained clinical interest and relevance due to their unique mechanical properties, biocompatibility, and biodegradability [1,2]. These materials present an alternative to inert metals such as titanium and stainless steel, which often necessitate secondary surgical procedures for removal after the healing process [3–5], which is inextricably associated with significant health care costs. The inherent biodegradability of magnesium alloys allows for gradual dissolution in physiological environments, thereby minimizing the long-term complications associated with permanent implants [6,7].

Mg-based implant screws — hereafter referred to simply as 'screws' or 'implants' interchangeably — used for bone fixation are biodegradable implants with growing prevalence and clinical application in orthopedic surgery. The Food and Drug Administration (FDA) has approved Mg alloy screws, used for fracture fixation that can safely dissolve within the body over time [8,9]. Clinical applications involve

Peer review under the responsibility of editorial board of Bioactive Materials.
* Corresponding author. Max-Delbrück-Centrum für Molekulare Medizin (MDC), Robert-Rössle-Straße 10, 13125 Berlin, Germany.
*E-mail addresses:* mostafa.berangi@mdc-berlin.de (M. Berangi), helmar@waiczies.de (H. Waiczies), Nandita.Saha@mdc-berlin.de (N. Saha), Shahriar.Shalikar@mdc-berlin.de (S. Shalikar), mahsa.salimi-majd@charite.de (M.S. Majd), thoralf.niendorf@mdc-berlin.de (T. Niendorf).

https://doi.org/10.1016/j.bioactmat.2026.05.001
Received 3 September 2025; Received in revised form 5 April 2026; Accepted 1 May 2026
Available online 16 May 2026

metallic fixation pins for use in oral surgery [10], anterior cruciate ligament (ACL) graft fixation screws [11,12] and compression screws for medial malleolar fracture fixation [13].

Bioactivity, biological response and tissue-material interactions are important design criteria for biodegradable implants [14]. However, monitoring the implantation site post-implantation is crucial for assessing healing progress and potential complications. This clinical need may introduce additional design criteria governed by characteristics inherent to the imaging modality and by the needs of patient safety [15–17].

Magnetic resonance imaging (MRI) is a mainstay of diagnostic imaging and enables non-invasive visualization of implants, degradation stage, and tissue integration free of ionizing radiation [18,19]. MRI provides means for tissue characterization, quantification of cell death, assessment of inflammatory processes, observation of bone growth and infection healing and for probing vascularization and tissue perfusion [20]. In addition to metallic implants, MRI has been applied to a range of bioactive material systems; for example, bimodal MRI/fluorescence imaging has been used in hydrogel-based proangiogenic implants to track in vivo degradation and vascular network formation, demonstrating that implantation mode and implant design significantly influence biological outcomes [21]. These studies demonstrated MRI's potential in monitoring various applications of biodegradable implants, ranging from local drug delivery to tissue engineering and angiogenic responses.

Safety of patients with electrically conductive passive metallic implants undergoing MRI is a critical concern, primarily due to the risks of radiofrequency (RF)-induced tissue heating [22]. This heating effect is due to the dipole antenna behavior of a passive electrically conductive implant when exposed to an external electromagnetic field and influenced by factors such as implant material properties, implant geometry and its orientation with respect to electromagnetic fields [23].

Metal-based biodegradable orthopedic implants present a particular challenge with respect to implant-induced RF heating. They not only share the limitations of inert metals such as titanium, but their degradable nature also results in a dynamic heating profile that evolves throughout the degradation process. As the implant structure changes over time, its electromagnetic response to RF exposure becomes structure-dependent, reflecting the ongoing material transformation. Understanding the kinetics and implications of the thermal effects of this interference warrants careful assessment to ensure patient safety during MRI. Implant induced heating of Magnesium-based biodegradable orthopedic implants in MRI has been examined empirically and benchmarked against Titanium equivalents *in vitro* [24] using few specific degradation states. Preliminary experimental studies showed that implant diameter, conductive cross-section, implant volume loss and surface roughness affect RF heating [24–27]. The conclusions drawn from these studies are valuable but constrained to the very specific experimental setup used. A systematic assessment of RF-induced heating of biodegradable implants remains uninvestigated. A thorough study of dynamic interference and thermal effects is difficult to perform *in vitro* and likely not feasible in vivo. However, advancements in state-of-the-art numerical electromagnetic field (EMF) simulations make this investigation feasible with unprecedented depth, accuracy and reproducibility [28,29].

Seizing this opportunity, the present study advances the state of the art by providing the first systematic investigation into the individual effects of key degradation parameters—including the presence of a fractured biodegradable screw—on the MRI-induced heating profiles of magnesium-based orthopedic screw implants.

This evaluation involves EMF simulations using a setup conforming to the test method F2182 of the American Society for Testing and Materials (ASTM) [30] and a clinically relevant human voxel model [31]. The findings derived from the EMF simulations are validated experimentally using test objects following the ASTM F2182.

By elucidating how specific degradation characteristics influence thermal responses during MRI, we offer new insights into the extent and nature of each parameter's contribution. This is achieved through a comprehensive suite of simulations that build upon, and extend beyond, previous anecdotal and preliminary experimental observations. The findings of this work have the potential to improve the safety and clinical performance of magnesium-based biodegradable screws during MRI, inform critical design criteria for future biodegradable implants, and support the development of next-generation orthopedic devices. This research is particularly relevant as the field moves towards more biocompatible and biodegradable materials that align with the principles of regenerative medicine and patient-centered care [32,33].

## 2. Methods

### 2.1. Corrosion mechanisms of Mg alloys

The corrosion of magnesium alloys, which results in shape deformation, proceeds through an electrochemical process involving two main interrelated reactions. First, magnesium undergoes anodic dissolution, where it oxidizes to release $Mg^{2+}$ ions. Simultaneously, water is reduced at the cathode to form hydroxide ions and hydrogen gas, which initially leads to the formation of a somewhat protective $Mg(OH)_2$ layer. However, in aggressive environments—especially those containing chloride ions—this film is disrupted, resuming the process. This process takes place with different kinetics at different implant locations. It results in volume reduction and the smoothing of sharp edges, accompanied by the development of a randomly rough surface that tends to expand laterally. This pitting behavior produces localized deep regions [34], induces changes in the electrodynamic properties of the degradation layer, and ultimately contributes to implant fissures and fractures. All mechanisms affect the interaction of biodegradable implants with electromagnetic waves, potentially leading to thermal effects.

### 2.2. Electromagnetic and thermal response to implant degradation

The geometrical and structural changes resulting from implant degradation can be categorized based on the different electromagnetic responses they induce. In this study, volume reduction and softening of sharp edges, surface roughening due to lateral pitting, formation of a degradation layer, and implant fracture are considered as critical parameters.

**Volume reduction and softening of sharp edges** influence the deposition of RF energy at implantation site through reduction of the electric field concentration which is directly proportional to the curvature of the conductor [35]. A common rule of thumb is that the local electric field ($E$) on a conductor is roughly inversely proportional to the local radius of curvature ($r$):

$$E \propto \frac{1}{r}$$

This is due to higher concentration of electrons in regions with higher curvature. The RF power deposition is expressed in terms of the specific absorption rate (SAR):

$$SAR \propto \frac{\sigma |E|^2}{\rho}$$

Where $\sigma$ is the electrical conductivity of the implant material, $E$ is electric field and $\rho$ is the density of the sample. Implant degradation smoothens the sharp edges of the implant leading to reduced $E$ fields which in turn reduce energy deposition in the implantation site.

**Surface roughening** alters the effective surface impedance of a biodegradable implant, thereby modifying the induced surface currents and, consequently, the undesired implant-induced electric and magnetic fields. The relationship between the tangential incident electric field ($E_t$), the surface current density ($J_s$), and the surface impedance ($Z_s$) is

governed by:

$$E_t = Z_s J_s$$

This expression indicates that, for a given incident electric field, an increase in the effective surface impedance will lead to a reduction in the induced surface current. These induced currents generate secondary electromagnetic fields focusing energy within the surrounding tissues. Modifications in $Z_s$ due to surface roughening can influence the local distribution of electromagnetic energy expressed in terms of SAR of RF energy in adjacent biological tissues.

**Changes in the electrodynamic properties of the degradation layer:** For Mg-based implants the degradation layer is primarily composed of $Mg(OH)_2$, a low-loss, insulating material with a relative permittivity of $\varepsilon_r \approx 3$ and relative permeability of $\mu_r \approx 1$. Reported thicknesses of this layer can reach up to 80 μm [36–38]. The formation of this degradation layer alters the boundary conditions at the implant/tissue interface by introducing an extra layer between the metallic surface of the implant and the surrounding tissues. The metallic portion of a biodegradable implant is responsible for conducting the RF-induced current, and its electrical properties, along with its structure, which defines the dipole behavior of the implant. Conversely, the degradation layer acts as a dielectric coating.

This coating, in turn, reduces the boundary of the conductive metal (i.e., the implant surface), resulting in a thinner pathway for electrical current. Consequently, the surface charge density on the screw increases, potentially leading to elevated electric fields and enhanced thermal effects in the immediate vicinity of the implant.

**Implant fissures and fractures** are a component of the corrosion process whereby an implant ultimately divides into two or more closely spaced segments. In this study, we focus on the case of a single fracture; however, the results can be extended to implants exhibiting multiple fractures. In contrast to a conventional electric dipole, the fractured implant demonstrates an electromagnetic response analogous to that of a fractionated dipole antenna [39]. Specifically, the fracture acts as a capacitive element, electrically coupling the separate segments of the implant. The capacitance ($C$) at the fracture site is directly proportional to the fracture cross-sectional area ($A$) and inversely proportional to the separation distance ($d$) [40]:

$$C \propto \frac{A}{d}$$

This localized capacitance generates an enhanced electric field ($E$), which scales with the induced current on the implant. Moreover, the magnitude of the induced current is determined by the implant's dimensions and the MRI resonance frequency—factors that collectively define the implant's antenna response [22]. Consequently, the equivalent capacitance at the fracture site functions as a tuning capacitor, thereby modifying the overall electromagnetic behavior of the implant. Depending on the implant, higher or lower values of $C$ can amplify the antenna response of the implant, making stronger $E$ that eventually induce higher SAR in the location of the fracture.

### 2.3. Degradation modeling of a Mg-based biodegradable orthopedic screw implant

Mg-based screws used for bone fixation are bio-degradable implants with growing prevalence and clinical application in orthopedic surgery. To emulate the corrosion and degradation of a Mg-based biodegradable orthopedic screw implant, a CAD model of a screw was created in STL format, where the surface is represented by triangles. Using this model, the progression of shape deformation due to chemical reactions between Mg and its environment was modeled through an iterative procedure, in which the volume of the screw model shrinks at each iteration, and the location and size of the surface triangles are adjusted to: 1) maintain the general shape of the model, 2) avoid overlap between iterations, 3) initiate pitting behavior at random locations and progress at the same locations during later iterations, 4) smooth sharp edges and 5) insert opening at locations where internal and external layers of the screw overlap each other. The degradation models generated are represented using surface triangles with a variable resolution from 30 μm up to 100 μm. The screw model used in this study is a compression screws with: L = 70 mm, D = 4.8 mm and guide wire diameter = 1.7 mm (Fig. 1).

Screw models V0–V7 (Fig. 1) were used in the simulations to investigate the effect of degradation-driven implant volume shrinkage on RF-induced heating. The remaining volumes at different degradation stages are reported in Table 1 as normalized values relative to the volume of the non-degraded screw (V0).

### 2.4. Electromagnetic field simulations

For 3D electromagnetic field (EMF) simulation the screw models made of pure Magnesium were exported into the (CST Studio Suite 2024, Dassault Systèmes). Broadband simulations were conducted using a transient Finite Integration Technique (FIT) [41] along with the frequency domain solver. The electromagnetic fields corresponding to the operating frequency of a clinical 3.0 T MRI scanner (f = 123.2 MHz) were recorded and used in the next simulation steps. The RF body coil deployed for RF excitation in the simulations followed the data provided by a MRI system manufacturer [42] where a cylindrical shield (L = 1500 mm and D = 752 mm) encompassing a generic high-pass birdcage coil (L = 713 mm and D = 450 mm) with 16-rungs in circular polarization was used. This setup enables cross study comparisons and serves as the foundation setup to assess the effect of degradation parameters while keeping all other factors the same.

Two simulation setups were examined. The first setup follows the guidelines provided by ASTM F2182 [30] where a phantom with electrical conductivity $\delta = 0.47$ S/m and dielectric constant $\varepsilon_r = 80$ with the dimensions L = 650 mm, W = 420 mm and H = 90 mm is placed at the center of the transmit RF body coil of the 3.0 T MRI scanner (Fig. 2). The screw implants are placed at the middle of the phantom with 30 mm distance from the side wall (Fig. 2).

For quantitative assessment of RF power deposition to the vicinity of the implant, the maximum SAR averaged over 1g tissue ($SAR_{1g,max}$) and point-SAR (SAR averaged over voxel) were recorded. EMF simulations were conducted with an accuracy of 1,35% $SAR_{1g,max}$ [43], resulting in a maximum mesh resolution of 200 μm, focusing on the region surrounding the implant. Numerical convergence was assessed by extrapolating $SAR_{1g,max}$ to infinitesimal mesh size as a function of mesh resolution (see Supplementary Fig. S1).

The second setup mimics a clinical scenario and involves EMF simulations in a realistic human voxel model [31]. Screw implants were placed into the tibia of the male human voxel model “Duke” (Fig. 2). Simulations were performed on the voxel model to estimate the behavior of the screw implants in vivo.

**Volume reduction:** CAD models of the screws (V0–V7) were incorporated into the EMF simulations using the ASTM F2182 phantom to quantify the effect of progressive implant volume loss on RF power deposition, expressed as $SAR_{1g,max}$. To more comprehensively evaluate how subtle geometric differences—arising naturally during corrosion—may influence RF interference and local SAR, an ensemble of shape-perturbed models was generated for each degradation volume. Starting from the baseline models V1–V7, nine additional variants were created per volume by introducing small, randomized geometric perturbations to the surface mesh. Specifically, every node of the surface triangulation was randomly displaced using a uniform distribution within a sphere of 0.04 mm radius. This perturbation amplitude was selected based on two criteria: (i) it introduces realistic stochastic deviations that mimic local, uncontrolled corrosion morphology, and (ii) it ensures that the global screw geometry and degradation stage remain unchanged, with total volume preserved within ±0.1% of the target volume state.

This ensemble-based approach (10 models per volume) allows

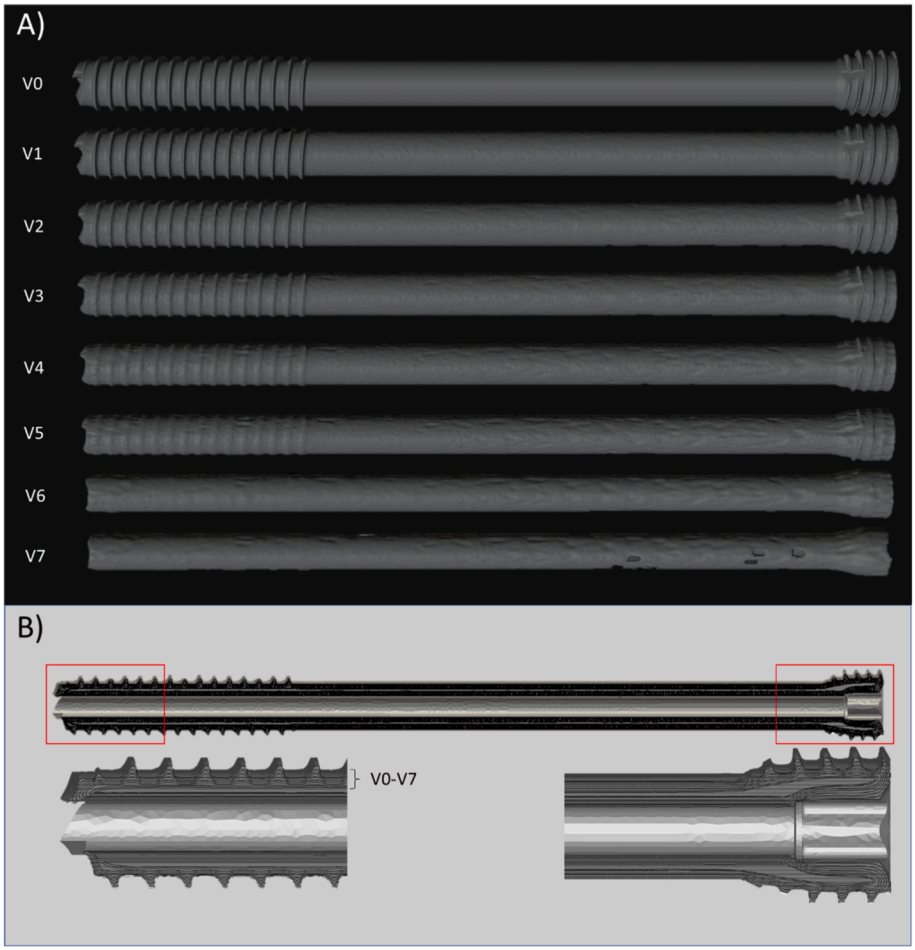


**Fig. 1.** Schematic view of the Mg-based screw model used in the electromagnetic field simulations. A) Volume reduction (V0-V7) corresponding to degradation time points of the 70 mm long screw model. B) An overlay of different degradation volumes (V0-V7) of the 70 mm screw, showing the cross-sections and border contours of the degraded screw samples.

**Table 1**
Relative remaining volume (%) of screws at distinct but arbitrary levels of degradation. The table compares 70 mm screw models, with degraded volumes (V1-V7) normalized to V0 (non-degraded model).

| Time point | Relative Volume% |
|---|---|
| V0 | 100% |
| V1 | 90% |
| V2 | 78% |
| V3 | 66% |
| V4 | 52% |
| V5 | 39% |
| V6 | 23% |
| V7 | 12% |

quantification of the variability in $SAR_{1g,max}$ attributable solely to naturalistic geometric differences rather than gross volumetric change. Notably, this is important because regions of high curvature and small-scale shape modulation strongly influence local electric-field enhancement and thus SAR. By sampling multiple realizations for each degradation stage, the simulations provide statistically robust estimates of SAR variability and ensure that conclusions about the effect of volume reduction are not dependent on a single, idealized geometric representation.

**Surface roughening:** The influence of corrosion-induced surface roughness on RF power deposition was modeled using the Hammerstad–Jensen formulation [44], which provides an impedance-based correction to account for the increased effective surface resistance of a conductor with non-smooth topography. In the electromagnetic solver, this correction was applied through the built-in function of the electromagnetic solver, enabling a direct modification of the metal's effective surface impedance without altering the underlying screw geometry. The root-mean-square (RMS) roughness amplitude was varied from 0 to 500 μm in 100 μm increments, spanning the range of surface features expected during intermediate and late-stage Mg corrosion. These values correspond to progressively more pronounced lateral pitting and micro-topographical irregularities that are commonly observed in biodegradable magnesium alloys.

To isolate the sole contribution of surface roughening—and avoid confounding effects from volume loss, edge smoothing, or degradation-layer formation—the simulations were performed using an otherwise non-degraded screw model with identical mesh resolution across all roughness conditions. $SAR_{1g,max}$ was computed for each roughness amplitude, allowing a controlled assessment of how increases in effective surface impedance modulate the induced current distribution and associated RF energy deposition in surrounding tissue.

**Degradation layer thickness:** The impact of the thickness of the degradation layer was examined by varying the thickness from 0 to 50 μm in 10 μm increments employing a non-degraded screw model. In the simulations, the corrosion layer is set to replace the surface of the screw, hence shifting the boundary of the metal. The simulations were performed to calculate $SAR_{1g,max}$ as a function of the degradation layer thickness.

The effect of the corrosion layer developing on the screw surface was

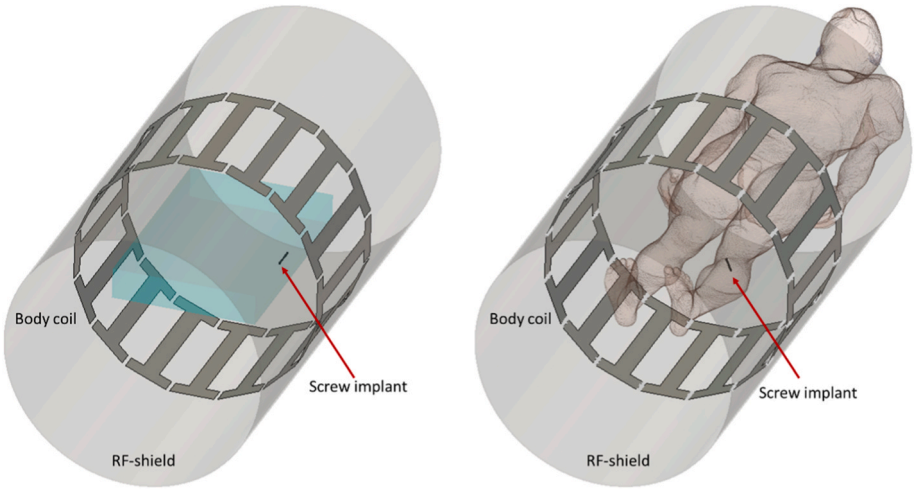


**Fig. 2.** Setup used for the electromagnetic field simulations including an RF-shield, a 16-rung high-pass body RF coil. left) For the simulations an ASTM-F2182 standard phantom containing a Mg-based screw implant (red arrow) was placed at the center of the superior-inferior direction with 30 mm distance from the side wall. right) For the EMF simulations mimicking a clinical scenario the human voxel model Duke was used with a screw implant placed in the tibia (red arrow).

evaluated by systematically varying the thickness of the magnesium hydroxide layer from 0 to 50 μm in 10 μm increments, using an otherwise non-degraded screw model to ensure that only the presence of the dielectric coating influenced the electromagnetic response. In the simulations, the degradation layer was implemented as a conformal dielectric shell that replaced the original metal–tissue interface, effectively shifting the conductive boundary inward while maintaining the external geometry. This approach captures a key physical consequence of corrosion-layer formation which is a reduction in the effective metallic cross-section available for RF-induced current flow. For each layer thickness, $SAR_{1g,max}$ was computed to quantify how incremental increases in dielectric-coating thickness influence local field intensification and energy deposition in adjacent tissue. This controlled parameter sweep provides a focused assessment of the electromagnetic implications of early-stage degradation-layer growth, independent of other concurrent degradation mechanisms.

**Fractures:** The influence of implant fractures on RF power deposition and thermal response was investigated by introducing controlled discontinuities along the screw and systematically varying their geometric characteristics. Depending on the simulation scenario, the fracture gap was filled with either ASTM F2182 phantom material or soft tissue, thereby representing both phantom-based validation and in-vivo conditions. The evaluated fracture parameters—width, surface pattern, orientation, and location—are illustrated in Fig. 3. To isolate the effect of each parameter, these factors were varied independently while all other model features, including mesh resolution and screw geometry, were held constant. The non-degraded screw (V0) served as the baseline reference for all comparisons.

Fractures oriented perpendicular to the screw's long axis ($\theta = 90°$) were first evaluated across a range of widths from 0.1 mm to 0.5 mm in 0.1 mm increments. For each width, $SAR_{1g,max}$ in the vicinity of the implant was computed to quantify how increasing capacitive discontinuity affects local field intensification. The effect of fracture surface pattern was assessed using a 0.2 mm-wide fracture located at the implant center. Ten randomized surface textures—each comprising irregular peaks and valleys with amplitudes up to ±0.1 mm (half the fracture width, ensuring no self-intersections)—were generated to emulate realistic, non-ideal fracture morphology. These were benchmarked against a smooth, planar fracture surface.

To evaluate orientation effects, the fracture angle θ was varied from 90° (perpendicular) to 30° in 10° decrements, using the same 0.2 mm-wide central fracture. $SAR_1g$ was recorded for each orientation and normalized to the $\theta = 90°$ condition to quantify how alignment with the primary induced current direction alters local energy deposition. Fracture location effects were examined by shifting a 0.2 mm-wide perpendicular fracture along the screw in 3 mm increments from one tip

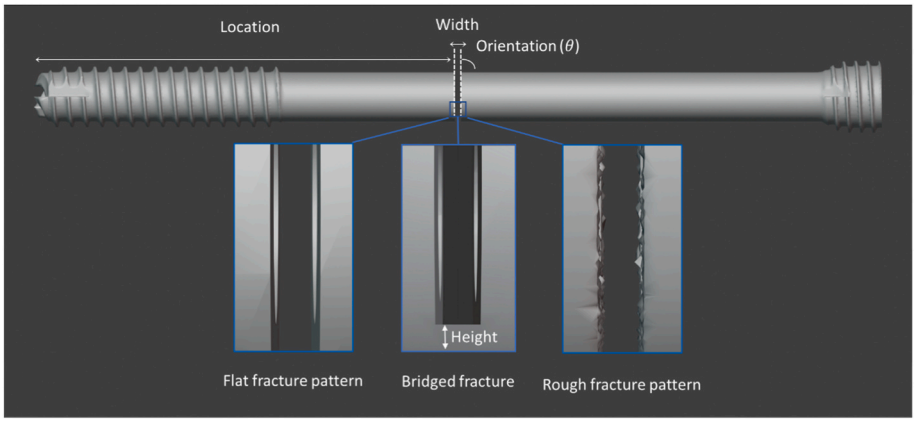


**Fig. 3.** Demonstration of fracture parameters including location along the long axis of the screw, orientation with respect to the long axis of the screw, fracture width, and textures. The texture includes: flat fracture, bridged fracture where two pieces of implant are connected along a bridge defined with its height and rough fracture.

to the other. Because $SAR_1g$ averaging can mask small, localized variations, maximum point-SAR was used as a more sensitive metric for this parameter sweep.

Finally, a clinically realistic "bridged fracture" configuration—where the two screw segments remain partially connected via a residual metallic bridge—was modeled using a 0.2 mm fracture at the center of the implant. Bridge height was varied to assess how partial electrical continuity modifies the implant's RF-induced current distribution and associated SAR patterns.

### 2.5. From SAR to temperature: experimental assessment of MRI heating of a biodegradable screw

MRI heating experiments were performed to validate the thermal simulations and to characterize the influence of implant fracture under controlled radiofrequency (RF) exposure. All experiments were conducted on a clinical 3.0 T whole-body MRI system (SkyraFit, Siemens Healthineers, Erlangen, Germany) using the integrated body RF transmit coil.

A rectangular phantom container (600 mm × 400 mm × 90 mm) was filled with the ASTM F2182-compliant gelled saline solution. The electrical properties of the phantom were verified before each measurement using a Dielectric Assessment Kit (DAK-12, SPEAG, Switzerland) to ensure that conductivity and permittivity remained within ASTM tolerance. After preparation, the phantom was sealed with a plastic cover to limit evaporative cooling and placed inside the MRI bore for a minimum of 24 h to allow full thermal equilibration with room temperature.

Fractured and non-fractured magnesium screws were suspended inside the phantom using a thin, non-conductive 3D-printed holder made of clear resin, which was submerged in the ASTM phantom gel (Fig. 4). The holder was designed to position the implant at a height of 45 mm above the phantom base and 30 mm from the side wall, while maintaining a small and consistent separation distance from the implant to reduce RF field perturbation. A non-conductive cotton string was used to secure the screw, avoiding any unintended electromagnetic coupling between the implant and the support structure. The same positioning protocol was applied for both fractured and non-fractured screws to ensure comparability across measurements.

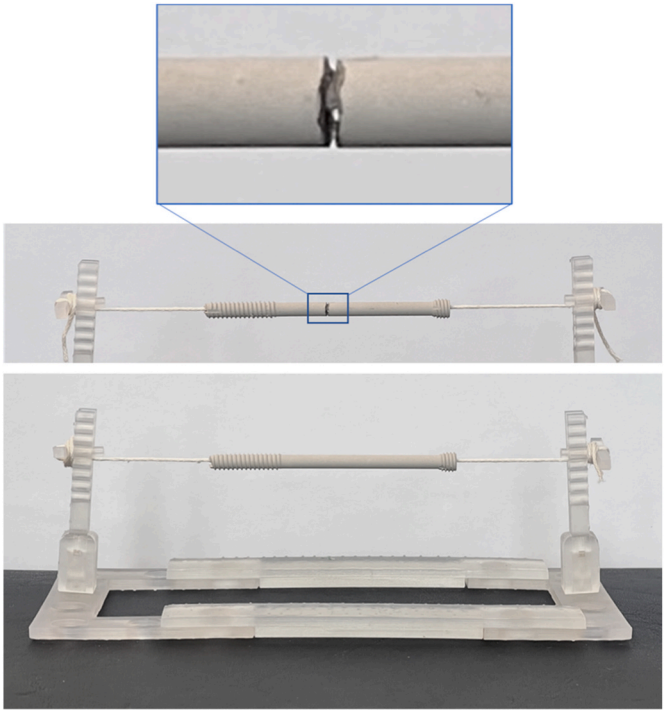

**Fig. 4.** Experimental setup used for validation of the temperature simulations. Screw holder setup used for phantom experiments of tissue heating due to implant fracture (zoomed view, top). A fractured implant and the exact non-fractured implant were used for MRI heating measurements. The screws are 70 mm long and are suspended in the phantom at a 45 mm distance from the bottom of the phantom. The material used to fill the phantom was prepared following the ASTM F2182 guidelines.

Temperature was recorded at the tips and center of the fractured and non-fractured implants using fiber-optic temperature sensors with ±0.1 °C accuracy (model T1, Neoptix Inc., Québec, Canada) and a temporal resolution of 1 s. The probes were tied to the implant holder using cotton strings, ensuring consistent contact without introducing conductive materials or adhesives.

RF heating was induced using a fast spin-echo sequence with a high RF duty cycle (TR = 5820 ms, TE = 6.8 ms, echo-train length = 8, RF refocusing flip angle = 120°, 24 slices, 20 averages). The scanner's internal RF calibration routine was used to set and maintain an input RF power of 97 W for a heating duration of 300 s. This protocol was performed twice: once with the fractured screw and once with the non-fractured reference implant. During each experiment, temperature was recorded continuously for the entire 300-s exposure period.

All aspects of the setup—including phantom composition, implant positioning, probe attachment, RF power calibration, and sequence configuration—were kept identical across experiments to ensure that observed temperature differences directly reflected the presence or absence of an implant fracture.

### 2.6. From SAR to temperature: thermal simulations of MRI heating of a biodegradable screw in a human voxel model

SAR, averaged over tissue masses, is the standard metric for RF safety in MRI according to IEC 60601-2-33 [45], but it does not fully represent local thermal effects, particularly near conductive implants where the metal's heat conductivity can alter the heating profile. To complement SAR-based assessment, we simulated RF-induced temperature rise around a biodegradable screw implanted in the left tibia using the Duke human voxel model.

The applied RF power corresponded to the IEC whole-body SAR limit of 2 W/kg, based on the model's mass (70.2 kg) and an absorbed-power fraction of ~30%. Temperature evolution was computed using the Pennes bioheat equation [46] with tissue thermal and perfusion properties from Duck [47], and electromagnetic loss density [48] as the external heat source.

Three configurations were simulated—intact screw, fractured screw, and a no-implant reference. The simulation assumed an ambient temperature of 293.15 K and a body temperature of 310.15 K. RF excitation was applied for 300 s, and the resulting temperature rise was recorded at 10-s intervals.

## 3. Results

### 3.1. $SAR_{1g,max}$ decreases with volume degradation of the biodegradable screw

Our simulations revealed that implant volume loss and smoothening of the sharp edges resulting from the structural degradation show a direct relation with $SAR_{1g}$ reduction. This is due to the fact that the electric field which is the main source of energy deposition in tissue is inversely proportional to the radius of the curvature. Hence, smoothening of the implant surface increase the radius of the curvature and therefore lowers the electric field, leading to a lower SAR. This result is in agreement with reports on MRI heating of magnesium based biodegradable screw implants [24]. A volume reduction of 48% resulted in a 4% decrease of $SAR_{1g,max}$ observed for the screw. An 88% degradation of the implant volume induced a 12% reduction in $SAR_{1g,max}$.

Fig. 6A shows the relative difference of $SAR_{1g,max}$ with respect to

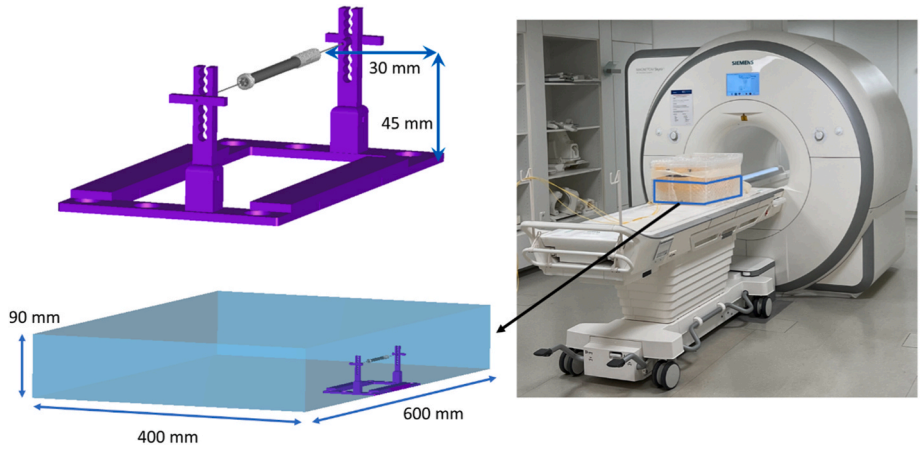


**Fig. 5.** MRI setup used for the experimental validation of the temperature simulations. The CAD model shows the implant holder placed inside of the phantom (for better visualization, the colors are different than real world). The 70 mm screw is suspended at 45 mm height and 30 mm distance from the side wall. The phantom material is 600 mm long, 400 mm wide and 90 mm high.

$SAR_{1g}$ of the non-degraded screw (V0), which serves as reference. For each degradation volume (V1–V7), a total of 10 screw models were considered in the simulations to capture the random variations in degradation patterns. The resulting $SAR_{1g,max}$ values for each volume are presented as grouped box plots.

### 3.2. Formation of degradation layer amplifies RF power absorption

During the early stage of the implant degradation, formation of the degradation layer has a marginal impact on the electromagnetic response of the screw implant. This is because the layer's thickness is 2-3 orders of magnitude smaller than the RF wavelength in tissue excited by clinical MR scanners with magnetic field strengths of 1.5T and 3.0T. Yet our simulations show for a degradation layer thickness of 50 μm an increment of 0.5% of relative difference of $SAR_{1g}$ with respect to the reference with no degradation layer. This minor increment is related to the reduction of the diameter of the screw as the degradation continues. As a result, the thinner conductor exhibits higher charge density due to the smaller surface area, resulting in a stronger E-field magnitude [40]. This elevated E-field will in turn increase maximum 1g-SAR [25,27].

Fig. 6B presents the relationship between the relative difference of $SAR_{1g,max}$ normalized to the reference with no degradation layer for various degradation layer thicknesses of magnesium hydroxide (degradation layer material). Increasing the degradation layer thickness is associated with a higher $SAR_{1g,max}$ with a linear response:

$$y = 0.079X, X \in [0, 0.05]$$

Where y represents percentage of the normalized relative difference of $SAR_{1g,max}$ and X represents the thickness of the degradation layer in mm. This relationship suggests that the presence of a thicker magnesium hydroxide layer enhances local energy absorption.

### 3.3. Increased screw surface roughness reduces RF energy absorption

Surface roughening results from random surface degradation patterns on the surface of the implant which expand laterally. We observed that higher surface roughness generally leads to lower $SAR_{1g,max}$. This occurs because greater surface roughness increases the surface impedance, leading to a lower induced current and therefore a lower implant induced electric field which in turn reduces $SAR_{1g,max}$ [26].

Fig. 6C displays the relative difference of $SAR_{1g,max}$ normalized to the $SAR_{1g,max}$ of the smooth implant as a function of the root mean square (RMS) surface roughness. A negative trend was found, where an increase of surface roughness leads to a decrease in $SAR_{1g,max}$ with the 0.5 mm (RMS) roughness resulting in 0.28% reduction of $SAR_{1g,max}$. This suggests that rougher implant surfaces reduce localized energy absorption, due to changes in the surface impedance of the implant. The data is best explained by a biexponential equation ($R^2 = 0.99$) with the parameters:

$$y = -0.2557e^{0.1819X} + 0.2583e^{-8.9454X}, X \in [0, 0.5]$$

Where y represents percentage of the normalized relative difference of $SAR_{1g,max}$ and X represents the surface roughness in mm.

### 3.4. Implant fractures introduce highest $SAR_{1g}$

The current induced on the implant due to RF excitation is responsible for the implant induced energy deposition in the tissues near the implant. The higher the magnitude of this induced current, the higher the energy deposition in the vicinity of the implant.

Implant fractures introduce a distinct electromagnetic behavior by effectively acting as a capacitive discontinuity in series along the implant. While this discontinuity acts as a barrier to the current flow, the capacitive behaviour leads to charge accumulation at the fracture site which in turn generates a new localized and concentrated electric field. This localized enhancement of the electric field can result in a higher local $SAR_{1g}$ inside the gap, potentially exceeding the SAR levels observed in the non-fractured implant.

Conversely, the fracture limits the magnitude of the induced current to a lower value in comparison to the non-fractured implant (Fig. 7). This is due to the increased total impedance of the implant caused by the fracture. This reduced current results in a reduced $SAR_{1g,max}$ in regions away from the fracture and a decrease in total energy deposition in the tissue surrounding the implant, averaged over any volume encompassing the entire implant. Overall, while the fracture may intensify localized energy deposition near the gap, it also mitigates global SAR risk by suppressing energy dissipation elsewhere along the implant. This section demonstrates the effect of different fracture parameters on local $SAR_{1g}$ along with the volume energy loss averaged over a 10 x 10 × 80 $mm^3$ volume. This volume is selected to be sufficiently large to encompass the energy deposition in tissue due to the implant.

Fig. 8A–F presents the relative differences in $SAR_{1g,max}$ and point-SAR (each normalized to the corresponding maximum SAR of the non-fractured implant) along with the volume loss over a 10 x 10 × 80 $mm^3$, and illustrate the effects of varying fracture width, fracture orientation, fracture location, and bridged fracture height, respectively. Fig. 8G shows the impact of a roughened fracture surface, expressed as the relative difference in maximum point-SAR compared to that of a fractured implant with a smooth fracture surface.

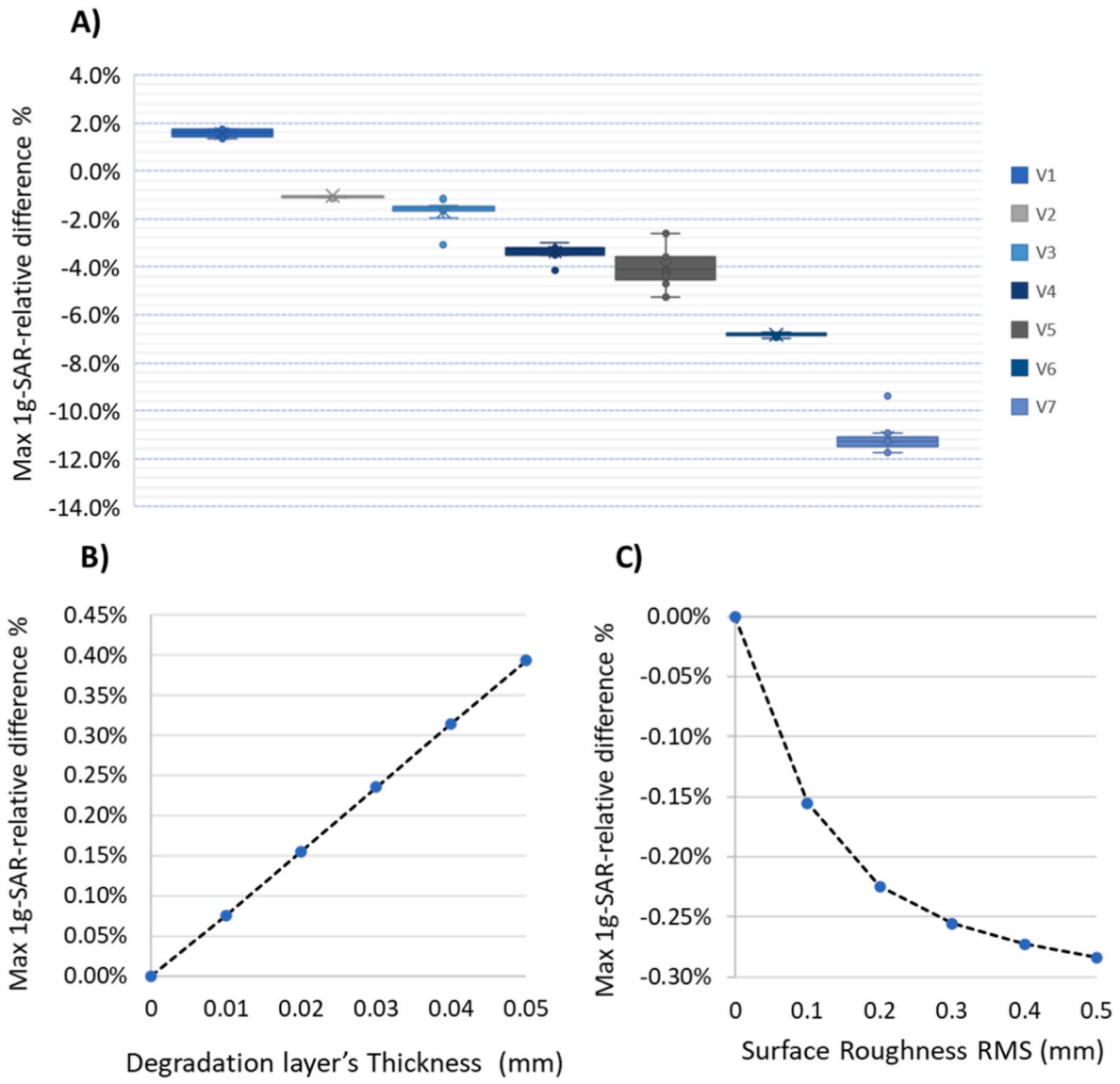


**Fig. 6.** Summary of results derived from the electromagnetic field simulations, A) Box-plots showing changes in $SAR_{1g,max}$ due to screw degradation. Each box represents the distribution of relative difference of $SAR_{1g,max}$ for 10 samples corresponding to randomly modified versions of the degradation volumes (V1–V7). Normalization is performed relative to the non-degraded screw (V0). Figures B and C represent the relative difference of $SAR_{1g,max}$ normalized to the intact implant as a function of B) magnesium hydroxide (degradation layer material) thickness and C) root mean square (RMS) of the surface roughness of the implant.

### 3.5. *Effect of the screw fracture width on $SAR_{1g,max}$*

Increasing the fracture width leads to higher impedance along the implant, which effectively reduces the induced current. The maximum energy deposition at each point in the space between the fractured ends (i.e., point-SAR) is proportional to the component of the induced current entering the fracture that is normal to the fracture plane. As the fracture width increases, the induced current decreases, resulting in lower energy deposition at the fracture site. Additionally, this overall reduction in induced current leads to a decrease in volumetric power absorption, averaged over a $10 \times 10 \times 80$ $mm^3$ region centered on the implant. Therefore, increasing the fracture width reduces both the localized energy deposition (point-SAR) at fracture location and the average power absorption across the entire implant region.

However, $SAR_{1g}$ at the fracture location does not follow the same trend as point-SAR, and is not constantly decreasing with the fracture width. This is because $SAR_{1g}$ is computed by averaging point-SAR over a 1-g tissue volume (approximately 1 $cm^3$). At smaller fracture widths, the electric fields—and thus the regions of elevated point-SAR—are confined within the narrow gap. As the fracture widens, peak point-SAR decreases, but the electric fields begin to spread over a larger region. As a result, $SAR_{1g}$ initially increases with fracture width due to this broader field distribution. Beyond a certain width, however, the continued decline in point-SAR outweighs the spatial spread, causing the $SAR_{1g}$ to decrease.

A visual animation provided in the supplementary document (GIF file in slide 1) illustrates the spatial distribution of energy deposition around the implant for different fracture widths, highlighting the variation in energy loss under each scenario.

Fig. 8A presents the relative difference in $SAR_{1g,max}$ normalized to the non-fractured implant. As the fracture width increases from 0 mm (no fracture) to 0.7 mm, $SAR_{1g,max}$ rises, peaking at a fracture width of 0.3 mm with a 19.1 % increase. Beyond this fracture width, further widening leads to a reduction in $SAR_{1g,max}$, with a width of 0.8 mm showing a 0.7% decrease relative to the non-fractured case. Fig. 8B presents the normalized volume energy loss, averaged over a $10 \times 10 \times 80$ $mm^3$ volume, as a function of fracture width from 0 mm (non-fractured implant) to 0.7 mm. A fracture width of 0.1 mm substantially

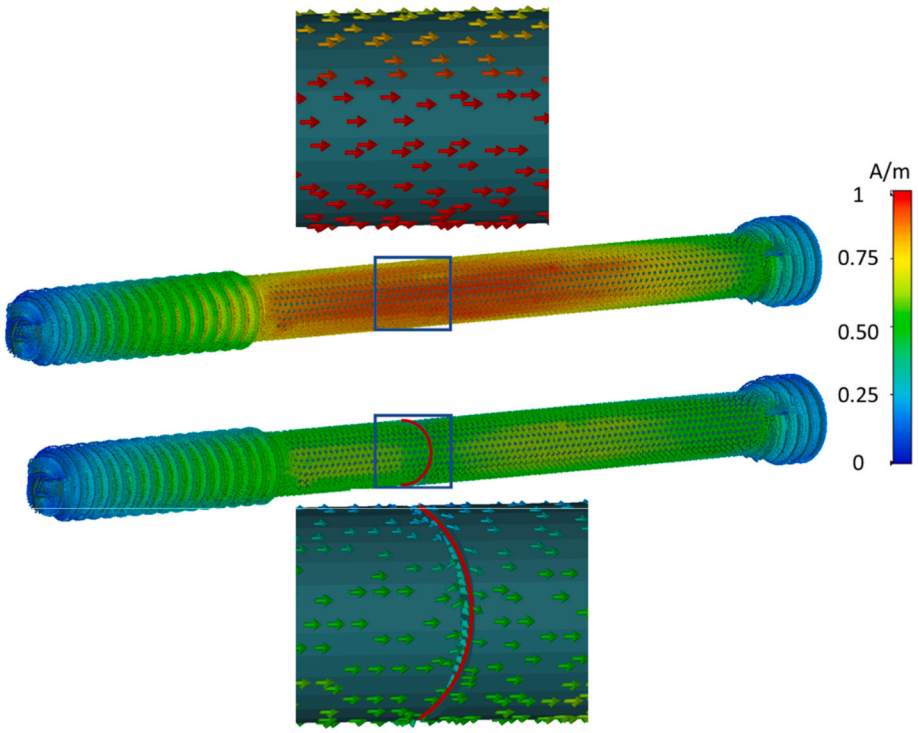


**Fig. 7.** Normalized RF-induced current profiles on the screw for a non-fractured implant (top) and a fractured implant (bottom), with the fracture cross-section highlighted in red.

reduces the volume energy loss to 66 % of the non-fractured value. The loss decreases steadily with increasing fracture width, reaching 37 % at a width of 0.7 mm.

### 3.6. Orientation-dependent $SAR_{1g}$ peaks in perpendicular screw fractures

As the fracture orientation angle (θ) decreases—where $\theta = 90^\circ$ corresponds to a 0.2 mm wide fracture perpendicular to the long axis of the screw—the impedance along the implant is reduced. This lower impedance increases the total induced current along the implant. However, the component of the current that is normal to the fracture plane decreases, since the induced current predominantly flows along the implant's axis as shown in Fig. 7. When the fracture is angled relative to the implant, the induced current is no longer perpendicular to the fracture plane, resulting in a weaker electric field across the fracture gap and, consequently, a lower $SAR_{1g}$ (and point-SAR) at the fracture site.

Despite this local reduction in energy deposition, the overall increase in induced current leads to higher power absorption averaged over a 10 × 10 × 80 $mm^3$ volume centered on the implant. Therefore, while reducing the fracture orientation angle reduces the localized $SAR_{1g}$ at the fracture, it simultaneously increases the volumetric power absorption in the surrounding tissue.

Fig. 8C shows the effect of the fracture orientation on the relative difference of $SAR_{1g,max}$ with respect to the reference of the non-fractured implant. As the orientation angle decreases, $SAR_{1g,max}$ decreases. The highest $SAR_{1g}$ occurs at $\theta = 90^\circ$, with a 17.4 % increase relative to the non-fractured case. A 10° decrease in orientation angle results in a 1.6% reduction in $SAR_{1g,max}$ compared to the $\theta = 90^\circ$, and this decreasing trend continues, reaching a 2.5 % reduction at $\theta = 30^\circ$ compared to the $SAR_{1g,max}$ of non-fractured implant. Fig. 8D shows the volume energy loss over a 10 × 10 × 80 $mm^3$ volume concentric with the implant, normalized to the value for the non-fractured implant. A perpendicular fracture exhibits the lowest volumetric energy loss, at 55 % of the non-fractured implant's value. The volumetric energy loss increases steadily as the fracture orientation (θ) decreases, with $\theta = 30^\circ$ showing the highest normalized loss at 66 %.

### 3.7. Shifting screw fracture location toward the center of the screw increases maximum Point-SAR

To investigate the effect of fracture location on RF power deposition, a 0.2 mm-wide fracture was systematically shifted along the length of the implant in 3 mm intervals. Because the $SAR_{1g}$ averaging volume (roughly 10 × 10 × 10 $mm^3$) can encompass multiple sampled fracture positions—thus reducing spatial resolution—the maximum point-SAR was used as a more sensitive and location-specific metric.

The simulations revealed that maximum point-SAR increases as the fracture moves from the implant tips toward its center. This trend is explained by the approximately sinusoidal distribution of the induced current along the implant, which peaks at the center. A fracture located near the center, acting as a capacitive discontinuity, experiences the highest current. Since the induced voltage—and thus the local electric field—is proportional to the current at the fracture site, a central fracture leads to a stronger electric field and, consequently, a higher point-SAR.

Fig. 8E shows the relative change in maximum point-SAR versus the non-fractured reference, as a function of fracture location. The implant center is defined at 0 mm, with negative values indicating positions toward the rear end of the implant. Our results demonstrate a clear dependency of point-SAR on fracture location, with the highest value occurring for the fracture being positioned at the center of the screw. In this case, the point-SAR increased by 472.3 % compared to the non-fractured reference.

### 3.8. Bridged screw fractures behave similar to non-fractured screws

The scenario where implant segments remain connected by a small bridging segment is presented in Fig. 8F. The relative difference of $SAR_{1g,max}$ normalized to the $SAR_{1g,max}$ of the non-fractured implant demonstrates a negligible effect on the RF power deposition. This behavior remains unchanged as the bridge height increases, suggesting that the presence of the bridging segment preserves the local energy absorption pattern of the non-fractured implant. The bridged segments

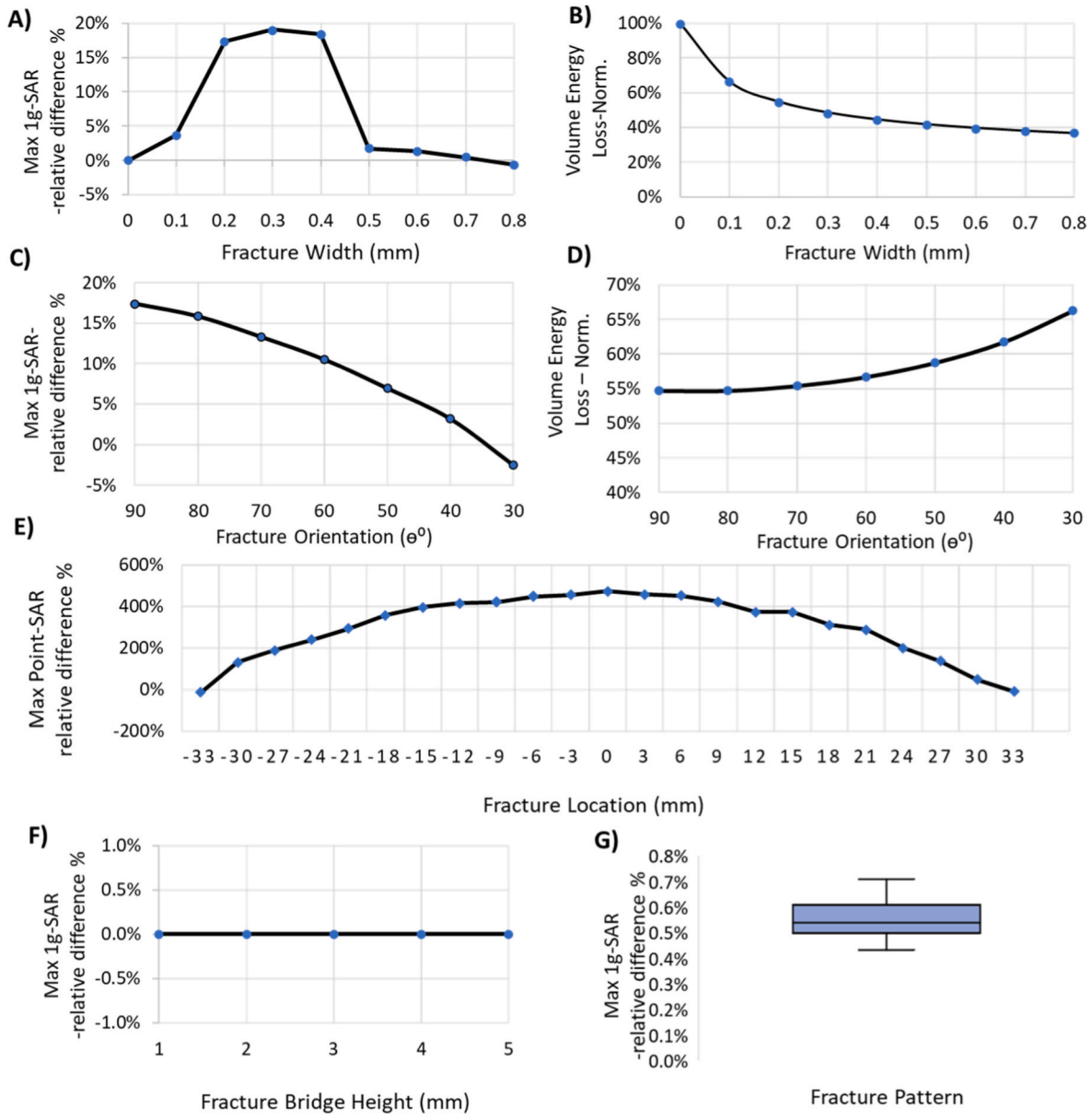


**Fig. 8.** SAR assessment for fractured implants showing maximum normalized difference SAR as a function of A and B) fracture width, C and D) fracture orientation, E) fracture location (with the center of the implant aligned to 0 mm), F) bridged fracture height, and G) fracture surface pattern based on 10 randomly generated rough fracture profiles. Figures B and D show averaged energy loss over a 10 x 10 × 80 mm3 volume and figure E shows maximum point-SAR, while the others present maximum 1g-SAR, all normalized to the corresponding value obtained for the non-fractured implant.

of the screw continue to function similarly to an intact implant, as the bridge maintains electrical continuity by allowing current to flow between the separated pieces.

### 3.9. Roughened screw fracture surface increases the maximum Point-SAR

So far, our results refer to a smooth fracture surface pattern. Next, we studied the impact of roughened fracture surface patterns, which showed an increase in $SAR_{1g,max}$ compared to a flat fracture surface pattern. This phenomenon is primarily due to the introduction of sharp edges on the fracture surface. The box-plot in Fig. 8G illustrates the distribution of the relative difference of $SAR_{1g,max}$ for 10 randomly generated fracture surface patterns, normalized to the $SAR_{1g,max}$ of a flat fracture, with all fractures positioned at the center of the implant using a fracture width of 0.2 mm. The variation in $SAR_{1g}$, with an average normalized rise of 0.56 %, suggests that fractured patterns increase the localized energy absorption. However, this increase was below 1 % for all of the investigated cases.

### 3.10. MRI-induced heating is reduced in fractured screw implants compared to non-fractured configurations

Temperature simulations were performed as a complementary step to the SAR simulations. While SAR quantifies the spatial distribution of RF energy deposition averaged over mass, temperature rise characterizes how this energy is dissipated within tissue. Furthermore, unlike SAR, temperature rise can be directly compared with experimental measurements for validation.

The simulated temperature time courses ($t$ = 0–300 s) for the fractured and non-fractured screw implants are presented in Fig. 9A and B, respectively. For the non-fractured screw implant, the greatest temperature rise occurred at the rear tip ($\Delta T = 3.96$ K), followed by the front tip ($\Delta T = 3.63$ K) and the center ($\Delta T = 1.82$ K). In the fractured implant, the maximum temperature rise was observed at the fracture site in the

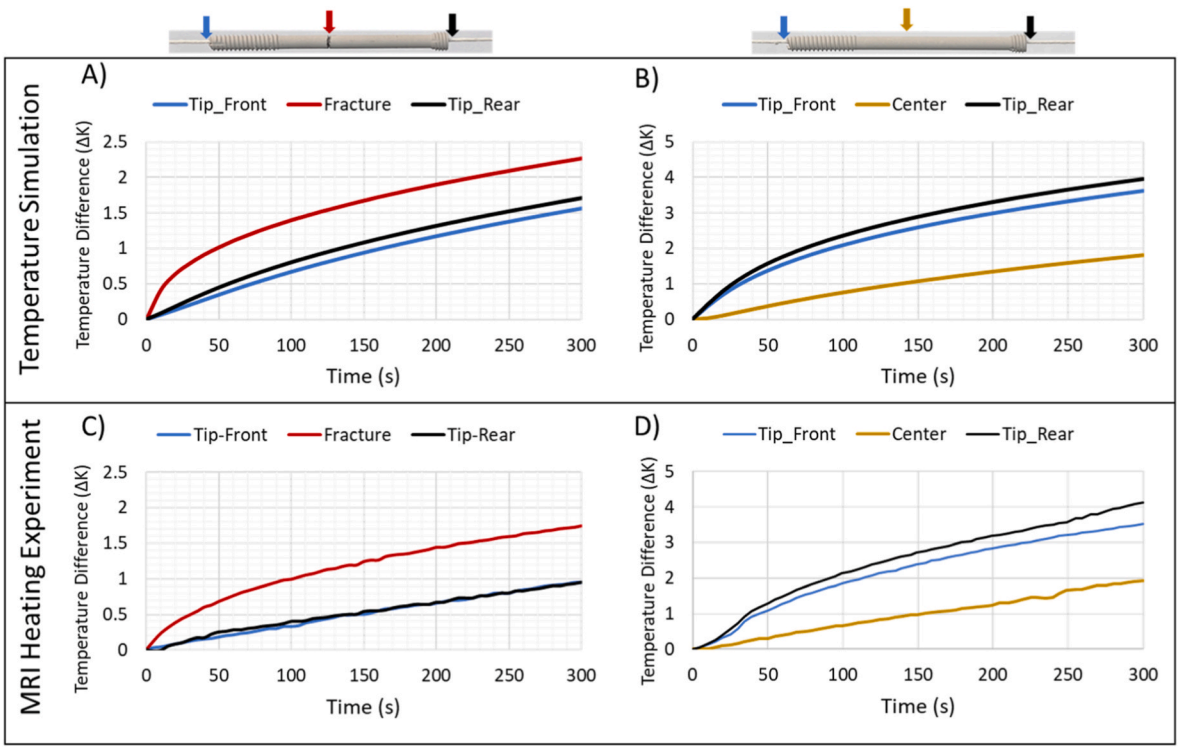


**Fig. 9.** Synopsis of the results obtained from temperature simulations (top) and from MRI heating experiments (bottom). Comparison of temperature increases at the tips (blue and black lines) and center (red or yellow lines) of a fractured and non-fractured screw implant. (A, B) Results derived from temperature simulations. (C, D) Corresponding results obtained from MRI heating experiments using a modified ASTM F2182 phantom. The implant's central fracture is illustrated in Figs. 4 and 5.

center ($\Delta T = 2.26$ K), with lower values at the rear tip ($\Delta T = 1.71$ K) and the front tip ($\Delta T = 1.56$ K).

Experimental validation of the temperature simulations was performed using MRI-based heating measurements in a dedicated phantom, following ASTM standards. The experimentally measured temperature time courses ($t$ = 0–300 s) for the fractured and non-fractured screw implants are shown in Fig. 9C and D, respectively. A detailed analysis of these experimental data revealed that, for the non-fractured screw implant, the largest temperature rise occurred at the rear tip ($\Delta T = 4.13$ K), followed by the front tip ($\Delta T = 3.52$ K) and the center ($\Delta T = 1.93$ K). For the fractured implant, the highest temperature rise was measured at the fracture site in the center ($\Delta T = 1.70$ K), with smaller increases at the rear tip ($\Delta T = 1.00$ K) and the front tip ($\Delta T = 0.90$ K).

### 3.11. *The fractured implant redistributes thermal energy, acting as a heat sink*

Although the $SAR_{1g}$ and point-SAR values are higher for the fractured implant than for the non-fractured one, our temperature simulations and heating experiments showed greater temperature elevation at the tips of the non-fractured implant.

To investigate the role of the screw implant's thermal conductivity on the temperature rise, an additional thermal simulation was performed. In this simulation, the power loss distribution from both fractured and non-fractured screw implants—placed inside the ASTM F2182 phantom—was imported into a temperature model as the heat source, but the screws themselves were excluded. This setup represents a scenario where the screw contributes no thermal conductivity, allowing heat to disperse solely through the phantom's thermal properties. The objective was to assess the screw's influence on temperature distribution.

Fig. 10A and 9B show simulations with fractured and non-fractured screw implants, respectively, while Fig. 10C and 9D depict simulations without screws. Color-coded arrows indicate locations where temperature elevation was tracked over 300 s at 5-s intervals. The temperature maps show that the screw helps distribute thermal energy along its length, with the fractured screw implant demonstrating more effective heat dissipation. This is because the material in between the fracture region, which induces the highest local SAR, is surrounded by the screw (metal with high thermal conductivity), allowing for better energy distribution and heat transfer to the phantom, thus preventing localized temperature spikes. In contrast, the non-fractured screw is less effective at heat distribution, resulting in more concentrated heating at its tips.

Additionally, Fig. 10C and D show that removing the screw—and thus eliminating its thermal conductivity—results in highest temperature rise in fracture region. The peak temperature reaches **$\Delta T$=14.1 $^0$C** for the fractured implant and **$\Delta T$=7.5 $^0$C** for the non-fractured implant, highlighting the screw's role in thermal distribution.

The results can be explained using heat transfer equation:

$$\frac{\partial T}{\partial t} \propto \nabla \cdot (k \nabla T) + Q$$

where T is temperature, k is thermal conductivity, and Q represents RF energy. Owing to its high thermal conductivity, the metallic implant rapidly redistributes the RF energy (i.e. local $SAR_{1g}$) along its length ($\nabla \cdot (k \nabla T)$), such that is efficiently conducted away and dispersed into the surrounding volume, thereby limiting local temperature elevation. In contrast, in the absence of the fractured implant, no conductive pathway exists to redistribute the deposited energy, leading to heat accumulation and the formation of a localized region of elevated temperature adjacent to the fracture site.

### 3.12. *Temperature rise in a human voxel model*

To mimic a clinical scenario a compressions screw (l = 70 mm) was placed into the tibia of the human voxel model Duke. The IEC 60601-2-33 guideline [45] limits the maximum local permissible temperature during MRI to 39 °C and 40 °C and the increase of the body core temperature to 0.5 °C and 1 °C for normal and first-level controlled

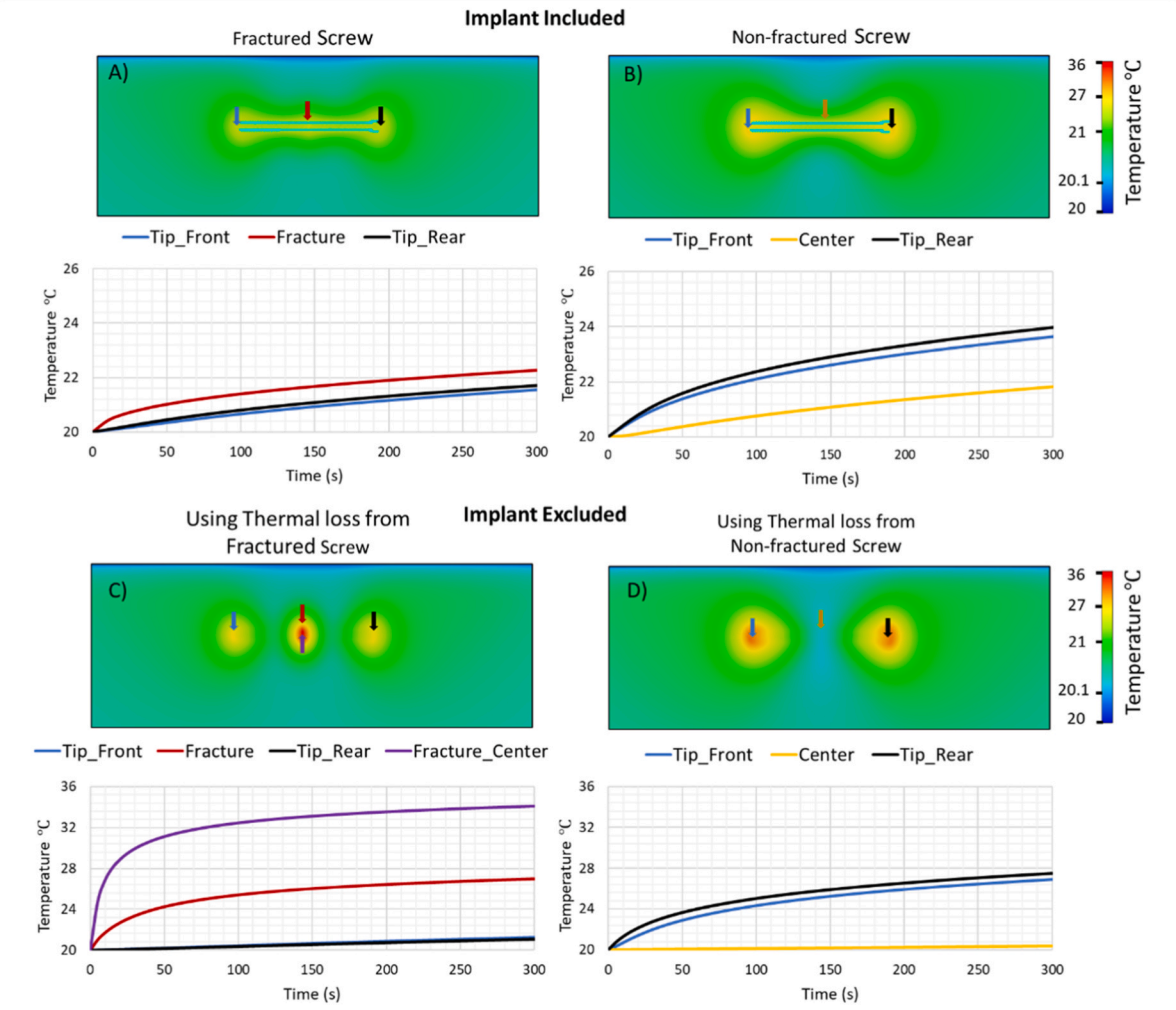


**Fig. 10.** Assessment of the influence of metal thermal conductivity on temperature distribution using thermal simulations. Color-coded arrows indicate the locations where the temperature time course was tracked over 300 s at 5-s intervals, with corresponding temperature evolution graphs shown below each temperature map. Temperature elevation maps correspond to: A) fractured screw implant, B) non-fractured screw implant, C) no screw (using power loss density from the fractured implant simulation), and D) no screw (using power loss density from the non-fractured implant simulation).

operation modes.

Our heating paradigm (97 W input power for a duration of 300 s) resulted in a whole-body SAR of 2 W/kg. With this RF power deposition, the temperature rise around the fractured implant remained below the 39 °C permissible limit for normal operation mode (Fig. 11). In contrast, the non-fractured implant reached temperatures up to 40.6 °C, exceeding the maximum temperature limit specified by the IEC 60601-2-33 guidelines.

## 4. Discussion

### 4.1. Key findings

To the best of our knowledge, this study is the first to provide a systematic, parameter-wise evaluation of degradation-related mechanisms and to quantify their individual effects on RF energy absorption and thermal responses of biodegradable magnesium-based screw implants under MRI exposure. The results demonstrate that implant degradation, whether through volume loss, formation of a degradation layer, changes in surface roughness, or mechanical fracture has a multifaceted impact on both the electromagnetic properties and the consequent thermal behavior of the device. These findings have major impact on the science and engineering of next generation of biodegradable implants.

The main contribution of the present work is its systematic modeling approach, which enables parameter-resolved analysis that is challenging - if not prohibitive - to achieve experimentally. Direct experimental validation of the EMF simulations is provided for fracture scenarios, as these can be reproducibly implemented, whereas isolating individual degradation mechanisms such as volume loss or surface roughness is extremely challenging because they evolve concurrently during *in-vitro* degradation. However, the trends derived from our simulations are in line with previous studies using specific experimental setups. These preliminary studies suggested that implant diameter and conductive cross-section affect RF heating [25,27] and indicated that increased surface roughness can reduce RF heating [26]. The observed reduction in SAR with implant volume loss is consistent with our experimental MRI heating measurements on biodegradable magnesium screws [24].

### 4.2. Degradation and electromagnetic response

Electrically conductive implants exposed to radiofrequency (RF) fields during MRI exhibit behavior analogous to that of dipole antennas. Consequently, structural changes occurring during degradation alter the electromagnetic response of the implant and, in turn, modify its MRI safety characteristics over time. Our findings show that a reduction in implant volume, accompanied by the smoothing of sharp edges, is associated with a decrease in maximum 1g-SAR. This effect is due to an

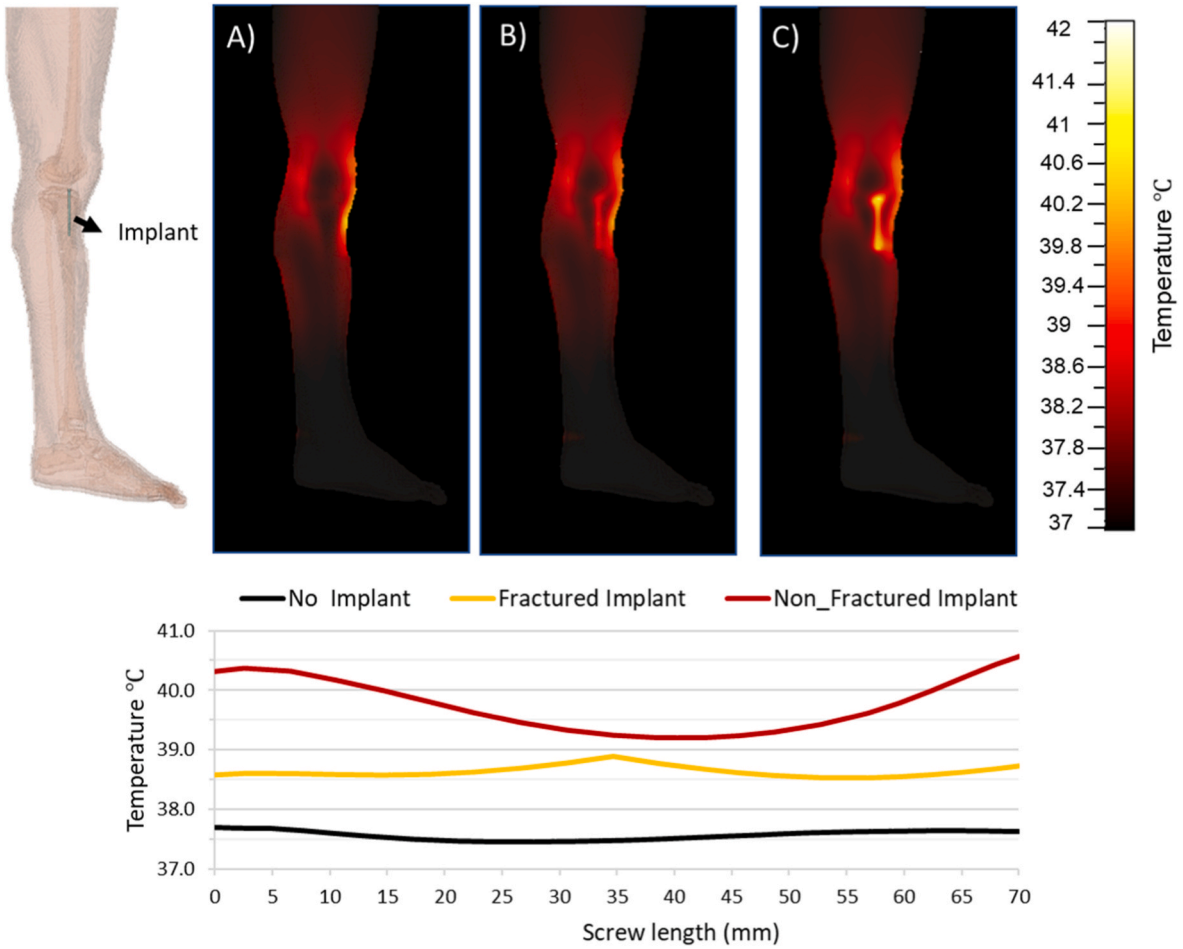


**Fig. 11.** Assessment of RF induced temperature changes for Mg based degradable screws (fractured and non-fractured) into the tibia of the human voxel model Duke. The figure shows the temperature increment map and corresponding temperature rise graph along the implant in the left leg of the voxel model for: A) no implant (black graph line), B) fractured implant (yellow graph line), and C) non-fractured implant (red graph line).

increase in the local radius of curvature, which reduces the concentration of electric fields at critical points. Interestingly, the formation of a degradation layer—primarily composed of magnesium hydroxide—results in only a slight increase in $SAR_{1g}$ (approximately 0.5% for a 50 μm layer), suggesting that even minor dimensional changes can influence charge distribution and local field intensity. Moreover, greater surface roughness appears to reduce 1g-SAR, due to the higher surface impedance, which impedes the flow of induced currents along the implant surface. These observations suggest that engineering the material to accelerate the degradation of sharp edges—resulting in a smoother, edge-free geometry (e.g., a screw losing its threads more rapidly)—while simultaneously promoting surface roughening during degradation could be an effective strategy for mitigating implant-induced heating during MRI.

### 4.3. Impact of fracture on SAR and thermal distribution

The presence of implant fractures introduces complex electromagnetic behavior by adding localized capacitance along the screw. The results demonstrate a non-monotonic relationship between fracture width and specific absorption rate (SAR). As the fracture width increases up to a certain threshold, the $SAR_{1g}$ remains higher than that of the non-fractured implant and reaches a peak within this range. Beyond this threshold, further widening of the fracture leads to a reduction in 1g-SAR. Additionally, fracture orientation influences 1g-SAR, with perpendicular fractures producing higher values. Fracture position also affects point-SAR, with centrally located fractures exhibiting higher point-SAR due to elevated current density, which follows a sinusoidal distribution along the implant. Furthermore, the bridged fracture does not modify the energy deposition pattern observed by the non-fractured implant.

Thermal simulations and MRI experiments complement the $SAR_{1g}$ and point-SAR findings derived from our numerical simulations. While fractured implants exhibit localized increases in SAR, they also show enhanced heat transfer capability. The presence of fractures leads to a more uniform redistribution of thermal energy along the implant, resulting in lower temperature elevations at the screw tips compared to intact implants. In the human voxel model, following 300 s of exposure to the maximum permissible RF power, the fractured implant, maintained temperatures below 39 °C, whereas the non-fractured implant surpassed the 40 °C safety threshold. To minimize the uncertainty budget of the simulations and of the experimental measurements and to ensure reliability of our data, several extra measures were taken. 1) The simulation accuracy was assessed by carefully examining the simulation uncertainty as a function of mesh size, as outlined in Supplementary Fig. S1. For a mesh size of 100 μm, an error of less than 1% was achieved. However, this mesh size would substantially increase the computational burden. To balance the trade-off between numerical accuracy and computational efficiency, a mesh resolution of 200 μm was used for all simulations, ensuring that the simulation error remains below 1.35% for $SAR_{1g,max}$ and supporting the reliability of our data. 2) For the experimental design and setup, we carefully followed the ASTM F2182 guidelines step by step to ensure the reliability and reproducibility of our data. Not only did we follow the ASTM guidelines, but we also validated

the electrical properties of the phantom gel used in the experiments by measuring permittivity and conductivity. This represents an additional step not required by the ASTM guideline and further supports the reliability of our data. 3) To ensure accurate and reproducible positioning of the screws during the experiments, we developed a thin, non-conductive 3D-printed holder made of clear resin, which was submerged in the ASTM F2182 phantom gel. The holder was designed to position the implant at a height of 45 mm above the phantom base and 30 mm from the side wall, while maintaining a consistent separation distance from the implant to reduce RF field perturbation. A non-conductive cotton string was used to secure the screw, avoiding any unintended electromagnetic coupling between the implant and the support structure. This holder also enabled accurate positioning of the fiber optic thermal sensors used for the temperature measurements, which have an accuracy of ±0.1 °C accuracy. 4) We ensured that the phantom was placed in the scanner room 24 h prior to the experiments to allow it to reach thermal equilibrium at room temperature and to minimize the potential impact of environmental temperature changes in the vicinity of the implant.

### *4.4. Mechanistic insights for material science and engineering and for clinical implications*

The observed reduction in SAR with volume degradation and increased surface roughness supports the concept of utilizing geometric modifications to effectively reduce the concentration of RF energy in surrounding tissue. Specifically, designing orthopedic implants with a higher degradation rate at the sharper edges, while maintaining the implant's load-bearing capabilities, could lead to a favorable reduction in tissue heating, thereby improving MRI safety. This approach could improve the transition of the implant towards less tissue-damaging phases more quickly, promoting safer outcomes during MRI procedures.

Furthermore, the thermal impact of fractures—by enhancing overall thermal distribution to surrounding tissues—suggests that intentionally engineered fractures or degradation features could offer thermal safety benefits. The role of the implant's thermal conductivity is especially significant; acting as a heat sink, the screw helps redistribute thermal energy, thereby preventing localized temperature spikes that could otherwise pose risks to surrounding tissues.

Furthermore, our findings indicate that the highest RF heating risk occurs shortly after implantation when the implant is intact, highlighting the importance of carefully designed MRI protocols used for post-implantation monitoring and potentially favoring a controlled degradation process to reduce long-term thermal risk.

To mechanistically link MRI safety with material composition, future designs of biodegradable implants should focus on increasing overall and surface impedance through targeted modifications of material chemistry and microstructure. Engineering materials to exhibit predefined bio-corrosion behavior to generate intentional, well-positioned fracture sites—strategically positioned based on RF interaction characteristics—may further enhance MRI safety. Such microstructural tuning would ensure that degradation proceeds along pathways that systematically diminish RF coupling and thermal risk.

To summarize, these findings have significant clinical implications for the design and evaluation of biodegradable passive metal-based orthopedic implants used in patients undergoing MRI.

### *4.5. Limitations and future directions*

While the present study offers insights into degradation-dependent electromagnetic and thermal responses of biodegradable screws, several limitations should be acknowledged. The electromagnetic field simulations were conducted using well-established human voxel models for MRI safety assessment; however, these models are based on discrete meshing and do not fully represent continuous anatomical structures, nor do they account for MRI-induced physiological variability. In addition, the experimental analyses employed idealized degradation profiles, which may not fully reflect the complexity and variability of degradation processes under clinical conditions. Nevertheless, the underlying concepts and trends illustrated in this study remain applicable across a range of degradation conditions.

## 5. Conclusion

This study systematically examined the influence of key degradation-related parameters on MRI-induced heating of biodegradable magnesium screw implants. Our findings indicate progressive degradation, including volume reduction and softening of sharp edges, reduces RF power deposition, with $SAR_{1g,max}$ decreasing by up to 12% at advanced degradation stages. Increased surface roughness further reduced $SAR_{1g,max}$ (0.28% at an RMS roughness of 0.5 mm), whereas formation of a magnesium hydroxide degradation layer had only a minor effect on RF power deposition (<0.5% change in $SAR_{1g,max}$). Although implant fractures increased localized $SAR_{1g,max}$ by up to 19.1%, simulations and MRI heating experiments demonstrated that fractured screws redistribute RF-induced heat more uniformly, resulting in lower peak temperature elevations compared with non-fractured screws. Importantly, these findings suggest that engineered degradation pathways—such as accelerated smoothing of sharp features or the incorporation of controlled fracture locations—could be intentionally leveraged to mitigate RF-induced heating, thereby improving the MRI safety profile of biodegradable orthopedic implants.

To conclude, our findings provide critical design criteria for biodegradable implants including a higher degradation rate of the sharp edges and intentional fracture points, aiming to promote the development of next-generation orthopedic implants that ensure effective biological resorption and minimal thermal risk during diagnostic MRI.

## CRediT authorship contribution statement

**Mostafa Berangi:** Writing – review & editing, Writing – original draft, Visualization, Validation, Software, Project administration, Methodology, Investigation, Formal analysis, Data curation, Conceptualization. **Helmar Waiczies:** Writing – review & editing, Methodology, Data curation. **Nandita Saha:** Writing – review & editing, Data curation. **Shahriar Shalikar:** Writing – review & editing, Visualization, Data curation. **Mahsa Salimi Majd:** Writing – review & editing, Visualization, Data curation. **Thoralf Niendorf:** Writing – review & editing, Validation, Supervision, Resources, Project administration, Methodology, Funding acquisition, Data curation.

## Ethics approval and consent to participate

No ethics approval was required.

## Funding sources

This work received funding from the MgSafe project, a European Union Horizon 2020 research and innovation program, under the Marie Skłodowska-Curie grant agreement No. 811226.

## Declaration of competing interests

The authors declare the following personal relationships which may be considered as potential competing interests: Thoralf Niendorf is CEO of MRI.TOOLS GmbH, Berlin, Germany.

## Appendix A. Supplementary data

Supplementary data to this article can be found online at https://doi.org/10.1016/j.bioactmat.2026.05.001.

## References


[1] J. Espiritu, M. Meier, J.-M. Seitz, The Current Performance of Biodegradable Magnesium-based Implants in Magnetic Resonance Imaging: a Review, 2021, pp. 4360–4367.

[2] S. Pina, J.M.F. Ferreira, Bioresorbable plates and screws for clinical applications: a review, J. Healthc. Eng. 3 (2) (2012) 846435.

[3] K.F. Farraro, K.E. Kim, S.L.Y. Woo, J.R. Flowers, M.B. McCullough, Revolutionizing orthopaedic biomaterials: the potential of biodegradable and bioresorbable magnesium-based materials for functional tissue engineering, J. Biomech. 47 (9) (2014) 1979–1986.

[4] L. Filli, R. Luechinger, T. Frauenfelder, S. Beck, R. Guggenberger, N. Farshad-Amacker, et al., Metal-induced artifacts in computed tomography and magnetic resonance imaging: comparison of a biodegradable magnesium alloy versus titanium and stainless steel controls, Skelet. Radiol. 44 (6) (2015) 849–856.

[5] S. Agarwal, J. Curtin, B. Duffy, S. Jaiswal, Biodegradable magnesium alloys for orthopaedic applications: a review on corrosion, biocompatibility and surface modifications, Mater. Sci. Eng. C 68 (2016) 948–963.

[6] D. Bian, J. Deng, N. Li, X. Chu, Y. Liu, W. Li, et al., In vitro and in vivo studies on biomedical magnesium low-alloying with elements gadolinium and zinc for orthopedic implant applications, ACS Appl. Mater. Interfaces 10 (5) (2018) 4394–4408.

[7] S. Ma, B. Zhou, B. Markert, Numerical simulation of the tissue differentiation and corrosion process of biodegradable magnesium implants during bone fracture healing, ZAMM - J. Appl. Mathem. Mech./Z. Angew. Math. Mech. 98 (12) (2018) 2223–2238.

[8] FDA US, FDA roundup: march 31, 2023 2023 [Available from: https://www.fda.gov/news-events/press-announcements/fda-roundup-march-31-2023.

[9] P. Newswire, Bioretec is the first in the world to receive FDA approval for a bioresorbable metal product www.prnewswire.com2023 [Available from: https://www.prnewswire.com/news-releases/bioretec-is-the-first-in-the-world-to-receive-fda-approval-for-a-bioresorbable-metal-product-301785531.html.

[10] Ž.P. Kačarević, P. Rider, A. Elad, D. Tadic, D. Rothamel, G. Sauer, et al., Biodegradable magnesium fixation screw for barrier membranes used in guided bone regeneration, Bioact. Mater. 14 (2022) 15–30.

[11] S. Stener, L. Ejerhed, N. Sernert, G. Laxdal, L. Rostgård-Christensen, J. Kartus, A long-term, prospective, randomized study comparing biodegradable and metal interference screws in anterior cruciate ligament reconstruction surgery: radiographic results and clinical outcome, Am. J. Sports Med. 38 (8) (2010) 1598–1605.

[12] K. Sundaraj, L.J. Salmon, E.L. Heath, C.S. Winalski, C. Colak, A. Vasanji, et al., Bioabsorbable versus titanium screws in anterior cruciate ligament reconstruction using hamstring autograft: a prospective, randomized controlled trial with 13-Year Follow-up, Am. J. Sports Med. 48 (6) (2020) 1316–1326.

[13] V. Herber, V. Labmayr, N.G. Sommer, R. Marek, U. Wittig, A. Leithner, et al., Can hardware removal be avoided using bioresorbable mg-zn-ca screws after medial malleolar fracture fixation? mid-term results of a first-in-human study, Injury 53 (3) (2022) 1283–1288.

[14] B. Xia, Y. Liu, Y. Xing, Z. Shi, X. Pan, Biodegradable medical implants: reshaping future medical practice, Adv. Sci. (Weinh.) 12 (35) (2025) e08014.

[15] J. Fritz, B. Lurie, H.G. Potter, MR imaging of knee arthroplasty implants, Radiographics 35 (5) (2015) 1483–1501.

[16] T.F. Raven, S. Boxriker, J. Mammadov, K. Petrov, A. Moghaddam, W. Friedl, Complications and imaging artifacts related to MRI in patients with intramedullary osteosynthesis after proximal femur fracture, J. Orthop. Surg. 27 (3) (2019) 2309499019879055.

[17] A.A. Oliver, E.K. Koons, P.S. Trester, J.E. Kleinow, R.S. Jonsgaard, A.J. Vercnocke, et al., Medical imaging compatibility of Magnesium- and iron-based bioresorbable flow diverters, AJNR Am. J. Neuroradiol. 44 (6) (2023) 668–674.

[18] M. Berangi, A. Kuehne, H. Waiczies, T. Niendorf, MRI of implantation sites using parallel transmission of an optimized radiofrequency excitation vector, Tomography 9 (2) (2023) 603–620.

[19] P. Yanev, G.A.F. van Tilborg, K.W.M. Boere, A.M. Stowe, A. van der Toorn, M. A. Viergever, et al., Thermosensitive biodegradable hydrogels for local and controlled cerebral delivery of proteins: MRI-based monitoring of in vitro and in vivo protein release, ACS Biomater. Sci. Eng. 9 (2) (2023) 760–772.

[20] J. Espiritu, M. Berangi, C. Yiannakou, E. Silva, R. Francischello, A. Kuehne, et al., Evaluating metallic artefact of biodegradable magnesium-based implants in magnetic resonance imaging, Bioact. Mater. 15 (2022) 382–391.

[21] A. Berdichevski, H. Simaan Yameen, H. Dafni, M. Neeman, D. Seliktar, Using bimodal MRI/fluorescence imaging to identify host angiogenic response to implants, Proc. Natl. Acad. Sci. 112 (16) (2015) 5147–5152.

[22] L. Winter, F. Seifert, L. Zilberti, M. Murbach, B. Ittermann, MRI-related heating of implants and devices: a review, J. Magn. Reson. Imag. 53 (6) (2021) 1646–1665.

[23] J. Wooldridge, A. Arduino, L. Zilberti, U. Zanovello, M. Chiampi, V. Clementi, et al., Gradient coil and radiofrequency induced heating of orthopaedic implants in MRI: influencing factors, Phys. Med. Biol. 66 (24) (2021) 245024.

[24] J. Espiritu, M. Berangi, H. Cwieka, K. Iskhakova, A. Kuehne, D.C. Florian Wieland, et al., Radiofrequency induced heating of biodegradable orthopaedic screw implants during magnetic resonance imaging, Bioact. Mater. 25 (2023) 86–94.

[25] C.J. Yeung, R.C. Susil, E. Atalar, RF safety of wires in interventional MRI: using a safety index, Magn. Reson. Med. 47 (1) (2002) 187–193.

[26] Enhancing skin-effect using surface roughening and its potential to reduce RF heating from implant leads, in: S. Seshadri, J.B. Scott (Eds.), Enzcon 2017, Electronics New Zealand Conference 2017, 2017, 2017; Christchurch, New Zealand.

[27] L. Winter, E. Oberacker, C. Özerdem, Y. Ji, F. von Knobelsdorff-Brenkenhoff, G. Weidemann, et al., On the RF heating of coronary stents at 7.0 tesla MRI, Magn. Reson. Med. 74 (4) (2015) 999–1010.

[28] On the accuracy of tier 4 simulations to predict RF heating of wire implants during magnetic resonance imaging at 1.5 T, in: P. Sanpitak, B. Bhusal, B.T. Nguyen, J. Vu, K. Chow, X. Bi, et al. (Eds.), 2021 43rd Annual International Conference of the IEEE Engineering in Medicine & Biology Society (EMBC), 2021 1-5 Nov. 2021.

[29] G. Bonmassar, P. Serano, MRI-induced heating of coils for microscopic magnetic stimulation at 1.5 tesla: an initial study, Front. Hum. Neurosci. 14 (2020) 53.

[30] A. Astm, F2182-11a Standard Test Method for Measurement of Radio Frequency Induced Heating near Passive Implants During Magnetic Resonance Imaging, ASTM International, West Conshohocken, PA, 2010.

[31] A. Christ, W. Kainz, E.G. Hahn, K. Honegger, M. Zefferer, E. Neufeld, et al., The virtual Family—Development of surface-based anatomical models of two adults and two children for dosimetric simulations, Phys. Med. Biol. 55 (2) (2010) N23.

[32] X. Zhang, Z. Hao, A novel device for studying in vivo magnesium degradation under controllable cyclic load in the rabbit model, J. Phys., Conf. Ser. 2468 (1) (2023) 012044.

[33] J. Nachtsheim, J. Burja, S. Ma, B. Markert, In vitro degradation behaviour of biodegradable magnesium alloys, Proc. Appl. Math. Mech. 22 (2023).

[34] G. Song, A. Atrens, Understanding magnesium corrosion—A framework for improved alloy performance, Adv. Eng. Mater. 5 (12) (2003) 837–858.

[35] D.F. Brailsford, A.J.B. Robertson, Calculation of electric field strengths at a sharp edge, Int. J. Mass Spectrom. Ion Phys. 1 (1) (1968) 75–85.

[36] X. Wang, Y. Fan, H. Chen, R. Yang, W. Zhao, Electrical, mechanical, and thermal properties of Mg(OH)2/PI nanocomposite films, J. Inorg. Organomet. Polym. Mater. 27 (6) (2017) 1778–1786.

[37] R. Rettig, S. Virtanen, Composition of corrosion layers on a magnesium rare-earth alloy in simulated body fluids, J. Biomed. Mater. Res. 88 (2) (2009) 359–369.

[38] L. Yang, N. Hort, D. Laipple, D. Höche, Y. Huang, K.U. Kainer, et al., Element distribution in the corrosion layer and cytotoxicity of alloy Mg–10Dy during in vitro biodegradation, Acta Biomater. 9 (10) (2013) 8475–8487.

[39] A.J.E. Raaijmakers, M. Italiaander, I.J. Voogt, P.R. Luijten, J.M. Hoogduin, D.W. J. Klomp, et al., The fractionated dipole antenna: a new antenna for body imaging at 7 tesla, Magn. Reson. Med. 75 (3) (2016) 1366–1374.

[40] C.A. Balanis, Antenna Theory: Analysis and Design, John wiley & sons, 2015.

[41] T. Weiland, A discretization model for the solution of Maxwell's equations for six-component fields, Arch. Elektr. Uebertragung 31 (1977) 116–120.

[42] A. Arduino, U. Zanovello, J. Hand, L. Zilberti, R. Brühl, M. Chiampi, et al., Heating of hip joint implants in MRI: the combined effect of RF and switched-gradient fields, Magn. Reson. Med. 85 (6) (2021) 3447–3462.

[43] A. Kuehne EO, H. Waiczies, M. Berangi, J. Nadobny, P. Ghadjar, P. Wust, T. Niendorf (Eds.), Parallel Transmit Local SAR Vs. Mesh Resolution in EMF Simulations of Highly Detailed Anatomical Models – a Rigorous Analysis, ISMRM, 2020.

[44] E. Hammerstad, O. Jensen (Eds.), Accurate Models for Microstrip Computer-Aided Design, IEEE MTT-S International Microwave symposium Digest, 1980, 1980 28-30 May 1980.

[45] I.E. Commission, IEC 60601–2-33:2022 Medical Electrical Equipment - Part 2-33: Particular Requirements for the Basic Safety and Essential Performance of Magnetic Resonance Equipment for Medical Diagnosis, 4.0 ed, IEC, 2022.

[46] H.H. Pennes, Analysis of tissue and arterial blood temperatures in the resting human forearm. 1948, J. Appl. Physiol. 85 (1) (1985) 5–34, 1998.

[47] F. Duck, Physical Properties of Tissues: a Comprehensive Reference Book, Academic press, 2013.

[48] K.R. Foster, R. Glaser, Thermal mechanisms of interaction of radiofrequency energy with biological systems with relevance to exposure guidelines, Health Phys. 92 (6) (2007) 609–620.